Eur. J. Mineral.
2003, **15**, 903–911

Dedicated to the memory of
Luciano Ungaretti

Topological analysis of the electron density of the clinopyroxene structure by the maximum entropy method: an exploratory study

MARCELLO MERLI [1,2*] and FERNANDO CÁMARA [2]

[1] Dipartimento di Scienze della Terra, via Ferrata 1, I-27100 Pavia, Italy
[2] CNR-Istituto di Geoscienze e Georisorse, sezione di Pavia, via Ferrata 1, I-27100 Pavia, Italy
* Corresponding author, e-mail: merli@crystal.unipv.it

Abstract: In the framework of a series of methodological studies to test the reliability of the reconstruction of the electron density distribution (EDD) by the maximum entropy method (MEM), we have attempted to check the possibilities of getting further information about the structural changes as a function of the chemical composition occurring in low-Ca clinopyroxenes by the analysis of the topology of the MEM EDD. The results of this study show that the topological analysis of MEM EDD yields results comparable to the bond critical points characteristics obtained in ground state EDD in minerals. Notable differences related to solid solutions have been found only at the M2 site of clinopyroxene structure. An attempt to describe the bond character at this site in the presence of significant solid solutions has shown differences related to chemical substitution that can be described in terms of variable ionicity. This result could be ultimately related to the different thermodynamic behaviour of the $P2_1/c \leftrightarrow C2/c$ phase transitions shown by chemically different clinopyroxenes. Since MEM can deal with experimental data on solid solutions, which cannot be treated with other available methods to reconstruct the experimental electron density, this approach opens new possibilities for the study of changes in the EDD topology of minerals with complex chemical substitutions.

Key-words: clinopyroxene, single-crystal X-ray diffraction, maximum entropy method, electron density topology.

1. Introduction

The characterisation of the atomic interactions between bonded nuclei (Bader & Essen, 1984) can be obtained by studying electron density maps. In these maps, the points where $\nabla\rho(\mathbf{r}) = 0$ are called critical points (c.p.), and a pair of atoms is bonded if and only if there exists a saddle critical point in the electron density between that pair of atoms (Bader, 1998). Rigorous topological analysis in Bader's sense (for a review see Bader, 1990) of experimental data should be carried out on electron densities obtained by multipolar refinement and/or ab-initio calculation (for a review see Coppens, 1997). Examples of multipole refinements can be found in the literature applied to inorganic and metallorganic materials (*e.g.* Ivanov *et al.*, 1999; Bianchi *et al.*, 2001) and minerals (some references are reported in Downs *et al.*, 2002). Studies of the bonding interactions in minerals by calculating electron density distributions (EDD) obtained by first-principles quantum mechanics can be found in Gibbs *et al.* (2001) and references therein.

The procrystal electron density, which is based on spherically averaged electron density distributions of non-interacting, static, ground state atoms placed at the positions that they occupy in the crystal, can be considered as reliable approximations of the "true" EDD. Despite being a non-bonded system, a study of the procrystal distribution of more than 300 metal-oxygen bonds in minerals provided the same bond critical points (bcp) and bcp properties as first principle calculations (Downs *et al.*, 2002), although differences were found in the sharpness of the curvature of the density perpendicular to the bond path. In addition, because of the nature of the procrystal model, ellipticities of the electron density in a cross-section perpendicular to a bond path are smaller than those obtained with first principle calculations, and provide little information about the stability of bonded interactions in the sense of Bader (1990).

When dealing with minerals, a solid solution is the common case in natural samples, involving chemical substitutions in one or more structural sites. Both multipolar reconstructions and ab-initio calculations are strongly dependent on the chosen model either in terms of choice of the appropriate wave function or in terms of the prior knowledge of the order/disorder scheme present in the real crystal; moreover, quantum-mechanical simulations of solid solutions are highly computational-demanding (see Dove, 2001 for some examples on pyroxenes). For these reasons we have attempted an MEM reconstruction of the EDD (Collins, 1982) instead of multipole refinement to access further information about one of the most frequent earth minerals, clinopyroxene. MEM calculations do not need any prior model on the short-long range spatial ordering of different components of the solid solution to compute the spatially-averaged

DOI: 10.1127/0935-1221/2003/0015-0903
0935-1221/03/0015-0903 $ 4.05

EDD, because it can be assumed that this information should be included in the experimental data. It is know that while *ab-initio* and multipole refinement of experimental data provide ground state EDD, MEM EDD are thermally smeared, unlike the ground state distributions. Nevertheless, our aim is to explore dynamic time- and space-averaged EDD in solid solutions of natural or synthetic clinopyroxene joins, in order to test the possibility of obtaining any information on the interactions between atoms which could be comparable with the traditional approach to the electron density studies.

Among the different natural compositions of clinopyroxenes, pigeonites have a further interest because they exhibit displacive phase transitions, which are reversible and composition-dependent (Brown *et al.*, 1972; Prewitt *et al.*, 1971; Sueno *et al.*, 1984). In pigeonite, a displacive $P2_1/c \leftrightarrow C2/c$ phase transition occurs at high temperature (Cámara *et al.*, 2002 and references therein) and with increasing pressure (Angel *et al.*, 1992; Hugh-Jones *et al.*, 1994), although H*P* and H*T* $C2/c$ structures are not equivalent. From a structural point of view, the phase transition is usually described as driven by changes in the arrangement of the chains of tetrahedra. In the $P2_1/c$ structure there are two different chains, A and B, while in the $C2/c$ structure the chains become symmetrically equivalent. In the high temperature $C2/c$ structure the two chains are extended, whereas in the high pressure form they are both kinked. These chain arrangements are also related to changes in the coordination of the M2 site. This fact implies that an accurate knowledge of the bonding interactions of the atoms involved in the structural changes may shed light on the driving mechanism and the physical principles responsible for the phase transition. Recently Downs (2003) has studied the topology determined from the procrystal EDD using available data in the literature about phase transitions in pyroxenes end-members in order to analyse topology changes in these compounds while changing *T* and *P*. His data show that each phase transition is coupled with a change in coordination of the M2 site. This is in line with the observations of Sueno *et al.* (1984) on the importance of the bonding around the M2 atom in the analysis of the mechanism of the pyroxene phase transition.

In this study, MEM has been applied to calculate the electron density maps starting from experimental sets of phased structure factors put in absolute scale. Such maps have been studied from the topological viewpoint, limiting the analysis to the search for the atom interactions between nearest-neighbour nuclei.

2. Mathematical analysis

2.1. Electron density calculation

We obtained dynamical electron density maps by entropy maximisation of the Shannon informational entropy *S* (Shannon & Weaver, 1949) defined as

$$S = \int_V \rho(\mathbf{r}) \ln\left(\frac{\rho(\mathbf{r})}{\tau(\mathbf{r})}\right) dV$$

(where $\rho(\mathbf{r})$ is the electron density to be calculated and $\tau(\mathbf{r})$ is some prior density), under the χ^2 constraint

$$\left(\frac{1}{M}\right)\sum_{k=1}^{M}\left(\frac{|Fo_k - Fc_k|}{\sigma_k}\right)^2 = 1$$

and

$$\int_V \rho(\mathbf{r})dV = F_{000}$$

where M is the number of unique reflections introduced, Fo_k the observed amplitude of the k^{th} reflection, Fc_k the corresponding value calculated via Fourier inversion of $\rho(\mathbf{r})$, and σ_k the experimental error associated with the k^{th} reflection.

Details on the crystallographic application of the Maximum Entropy Method can be found in Collins (1982), Prince (1988), Price *et al.* (1989), Sakata & Sato (1990). An extensive review of the method employed in solving crystal structures can be found in Bricogne (1984).

A home modified version of the routine written by Kumazawa *et al.* (1993) has been adopted.

Working with the present data, we realised that the MEM method starting from a flat map (*i.e.* $\rho(\mathbf{r})=F_{000}/V$ everywhere) and involving experimental data sets with resolution up to $\sin(\theta)/\lambda = 1.1$ does not yield good results, as pointed out by Jauch & Palmer (1993). The amount of information contained in such a resolution shell is not enough to model the electron density at the nuclear positions, and this feature consequently involves a bias in the low-density regions.

A study in order to improve the MEM solution is in progress at our lab. In order to overcome the problem of the data truncation in the present work, the MEM process was started with a prior information instead of a flat map, *i.e.* a theoretical distribution obtained from a very large number of calculated structure factors (up to $\sin(\theta)/\lambda = 1.8$). The structure factors used to obtain the prior EDD were calculated both from the model obtained by structure refinement, using spherical scattering forms and harmonic thermal motion, and by Fourier inversion of a theoretical procrystal (dynamicised) map. The introduction of the higher resolution information in the MEM process actually yields a significant improvement of the electron density estimation on the nuclear positions, with consequent unbiased determination of the low-density zones.

This approach had been previously studied and criticised by Roversi *et al.* (1998) and Palatinus & Van Smaalen (2002). In order to investigate in an exploratory sense the capabilities of the MEM reconstruction of the dynamical electron density in such studies, we have considered as an acceptable approximation for this preliminary work the use of such a prior density. Further details on prior knowledge in the ME method are in progress (Merli *et al.*, in prep.).

In order to obtain a symbolic representation of the electron density calculated with the above-mentioned routine, the λ coefficients of the MEM function

$$\rho(\mathbf{r}) = \exp\left(\sum_{k=1}^{M}\lambda_k \exp(-2\pi i(\mathbf{h}_k\mathbf{r}))\right)$$

have been calculated via Fourier inversion of $\ln[\rho(\mathbf{r})]$ (Merli *et al.,* 2002b). This symbolic representation of the MEM EDD allowed us to implement the MEM electron density calculation in the code of a locally modified version of the SPEEDEN program (Downs *et al.*, 1996), kindly provided by R.T. Downs.

2.2. Topological analysis

As mentioned above, a good introduction on this matter is presented in Bader (1990) and, for mineralogical applications, in Gibbs *et al.* (2001) and Downs *et al.* (2002). We would just like to recall here some crucial points, which could have some importance with respect to the present work.

According to Bader & Essén (1984), the analysis of $\nabla^2\rho(\mathbf{r})$ at the bond critical points (*i.e.* where $\nabla\rho(\mathbf{r})=0$) can yield the following kind of topological situations:

1. $\nabla^2\rho(\mathbf{r}) < 0$: there is a local concentration of charge at c.p., *i.e.* a "shared interaction" or a covalent linking.
2. $\nabla^2\rho(\mathbf{r}) > 0$: there is a local depletion of electrons, typical for "closed-shell interaction", or an ionic bond.

In optimised diatomic hydride MH molecules, as $\rho(\mathbf{r})$ increases in value and the MH bonds decrease in length, the sign of $\nabla^2\rho(\mathbf{r})$ changes from positive to negative and its values are progressively larger in magnitude (Gibbs *et al.*, 2001). However, in silicates there is a positive correlation between $\rho(\mathbf{r})$ and $\nabla^2\rho(\mathbf{r})$. Hence, a general assessment of the bond character on the basis of the sign of $\nabla^2\rho(\mathbf{r})$ in minerals can lead to disparate results (Gibbs *et al.*, 2001). Maybe this criterion for characterising the chemical bond is no longer reliable and requires some revision. We do not want to argue about these questions, and this paper would merely like to represent a preliminary presentation of the results rather than an interpretative criticism of the matter.

We must point out two peculiar features of our samples that make the "traditional" results of a topological analysis somehow different: i) we are dealing with solid solutions; ii) our maps are time-averaged, and thus some considerations must be made.

With respect to point i), the electron density evaluated as an average on a unit cell does coincide with the "true electron density" if the whole crystal (*i.e.* all of the cells) is chemically homogeneous. When a solid solution occurs, the electron density would represent a "spatial average" of different unit cells, whose actual distribution in the crystal is not known. Thus the chemical bond paths that one can investigate do not represent actual chemical bonds, since the bond path is a local property. In this paper we just present the features of these "bond paths" in the presence of a solid solution, treating them as a true chemical bond.

Regarding ii), it is well known that MEM reconstruction of the electron density cannot itself provide the ground-state distribution of the electrons, and its deconvolution is not so straightforward. However, the topological analysis can be performed even on a time-averaged object such as the MEM dynamical electron density (*cf.* Bader, 1990, p. 7). Thus, some differences between a static and a dynamical map should be found even if non-degenerate bcp's found in a ground-state map must also be found in a dynamical one (Morse c.p's).

In order to qualitatively investigate the influence of the nuclear motion on the electron density distribution at the c.p. points, the following test has been performed: starting from a static procrystal map of a pure diopside, the corresponding dynamical map (obtained by convolution with gaussian probability functions on the basis of the crystallographic structure refinements) has been studied in terms of the topology of the bond directions, following Bader. This dynamical map has also been used as prior information for the MEM reconstruction of the EDD of diopside using experimental structure factors.

Table 1. Unit-cell parameters and refinement results.

Crystal		BTS-308 n.13	Dien2
CNR-IGG identification code		*hdn*	*hjt*
Space group		$P2_1/c$	$P2_1/c$
Unit cell dimensions	*a* (Å)	9.716(3)	9.651(2)
	b (Å)	8.948(4)	8.846(2)
	c (Å)	5.250(3)	5.202(1)
	β (°)	108.49(4)	108.38(2)
Volume	(Å^3)	432.89(4)	421.5(3)
Theta range for data collection		2.2 – 55.1 °	2.0 – 45.1 °
Independent reflections		5549	3495
$R_{(int)}$		0.028	0.045
Final *R* indices [I>3σ(I)]		0.0387	0.0433
R indices (all data)		0.0601	0.0597

3. Experiments

3.1. Samples and preparation

Two pigeonite crystals were selected: a sample labelled "Dien2", which is iron-free and was synthesised and studied by Tribaudino *et al.* (2002). Its composition is $[Ca_{0.15(1)}Mg_{1.85(1)}][Si_{2.00(1)}]O_6$. The second, a natural one, labelled as BTS-308 N.13, is iron-bearing with a composition close to $[Ca_{0.19(1)}Mg_{0.91(1)}Fe_{0.86(1)}Mn_{0.03(1)}Ti_{0.01(1)}][Si_{1.97(1)}\ Al_{0.03(1)}]O_6$. The origin is a ryodacite sample from Paranà (Brazil). This is a Ca-rich pigeonite sample free of augite exsolutions that has been already studied by Cámara *et al.* (2002) and references therein.

3.2. X-ray single crystal data collection and structure refinement

Data collections and structure refinement strategies are described in Merli *et al.* (2002a). Unit cell parameters and information on data collections and structure refinement are reported in Table 1. The final positional and anisotropic displacement parameters are reported in Table 2, which is available on request from the authors. A maximum residual electron density at a distance of 0.43 Å from the M2 site was observed for crystal BTS-308 n.13 in the Fourier-difference synthesis. The same feature was observed in crystal Dien2 at 0.55 from the M2 site. A maximum at the same position was observed using low resolution high-temperature data of crystal BTS-308 N.16 (Cámara *et al.*, 2002) and high resolution diffraction data of crystal Dien2 (Tribaudino & Nestola, 2002).

4. Results and discussion

Comparison of MEM EDD and procrystal EDD topologies on diopside

For the comparison of the EDD's obtained using a procrystal model, the corresponding dynamical map, and the MEM

Table 3. Bond-critical point properties for diopside for the procrystal, dynamic procrystal and MEM EDD's. The values of $\rho(\mathbf{r})$ (e/Å^3), of $\nabla^2\rho$ (e/Å^5), fractional coordinates, bond-lengths (Å), eigenvalues of the hessian matrix (e/Å^5), and the ratios $|\lambda_1|/\lambda_3$ are also given.

Procrystal EDD

	$\rho(\mathbf{r})$	$\nabla^2\rho(\mathbf{r})$	x	y	z	d	$\lambda1$	$\lambda2$	$\lambda3$	$\lvert\lambda_1\rvert/\lambda_3$
SiO1	0.88	20.45	0.2128	0.0908	0.1919	1.600	-4.47	-4.46	29.38	0.15
SiO2	0.90	21.72	0.3187	0.1608	0.2683	1.586	-4.73	-4.71	31.17	0.15
SiO3	0.77	14.72	0.3136	0.0610	0.1296	1.669	-3.35	-3.33	21.41	0.16
SiO3	0.75	13.42	0.3137	0.0463	0.3427	1.687	-3.10	-3.08	19.61	0.16
M1O1	0.24	4.36	0.0507	0.9878	0.2012	2.120	-0.80	-0.78	5.95	0.13
M1O1	0.26	5.38	0.0512	0.9104	0.4246	2.061	-1.01	-0.99	7.38	0.14
M1O2	0.26	5.40	-0.0614	0.8374	0.2812	2.057	-1.02	-1.00	7.43	0.14
M2O1	0.23	4.18	0.0587	0.1924	0.1943	2.364	-0.80	-0.78	5.76	0.14
M2O2	0.24	4.45	0.0710	0.2774	0.4705	2.344	-0.89	-0.80	6.13	0.15
M2O3	0.16	2.48	0.0788	0.4056	0.3854	2.564	-0.43	-0.31	3.23	0.13
M2O3	0.12	1.56	0.0766	0.3966	0.1399	2.721	-0.26	-0.18	2.00	0.13

Dynamic procrystal EDD

	$\rho(\mathbf{r})$	$\nabla^2\rho(\mathbf{r})$	x	y	z	d	$\lambda1$	$\lambda2$	$\lambda3$	$\lvert\lambda_1\rvert/\lambda_3$
SiO1	0.89	25.91	0.2098	0.0905	0.1918	1.600	-6.19	-5.02	37.12	0.17
SiO2	0.91	22.23	0.3202	0.1630	0.2715	1.586	-5.87	-5.85	33.95	0.17
SiO3	0.75	19.62	0.3156	0.0595	0.1263	1.669	-5.38	-4.20	29.28	0.18
SiO3	0.74	17.94	0.3142	0.0441	0.3474	1.687	-4.51	-3.56	26.01	0.17
M1O1	0.27	1.92	0.0536	0.9842	0.2030	2.119	-1.22	-0.88	4.01	0.30
M1O1	0.24	4.24	0.0538	0.9148	0.4195	2.061	-0.77	-0.39	5.40	0.14
M1O2	0.27	3.55	-0.0639	0.8418	0.2819	2.057	-1.31	-0.56	5.41	0.24
M2O1	0.25	1.11	0.0618	0.1950	0.1996	2.364	-1.21	-0.88	3.20	0.38
M2O2	0.23	3.01	0.0728	0.2786	0.4604	2.345	-0.92	-0.67	4.60	0.20
M2O3	0.18	2.04	0.0732	0.4209	0.3570	2.564	-0.48	-0.12	2.59	0.19
M2O3	0.18	0.97	0.0862	0.3988	0.1703	2.720	-0.27	-0.19	1.44	0.19

MEM EDD

	$\rho(\mathbf{r})$	$\nabla^2\rho(\mathbf{r})$	x	y	z	d	$\lambda1$	$\lambda2$	$\lambda3$	$\lvert\lambda_1\rvert/\lambda_3$
SiO1	0.84	29.03	0.2096	0.0909	0.1891	1.600	-3.57	-2.92	35.52	0.10
SiO2	0.93	24.90	0.3220	0.1628	0.2679	1.586	-7.10	-3.71	35.72	0.20
SiO3	0.76	16.67	0.3141	0.0564	0.1270	1.669	-6.37	-5.65	28.69	0.22
SiO3	0.75	18.41	0.3198	0.0411	0.3408	1.687	-4.60	-3.22	26.23	0.18
M1O1	0.26	3.15	0.0525	0.9779	0.1882	2.120	-0.75	-0.43	4.33	0.17
M1O1	0.25	2.36	0.0519	0.9184	0.4230	2.061	-1.29	-0.79	4.44	0.29
M1O2	0.26	3.07	-0.0525	0.9779	0.3118	2.119	-0.78	-0.46	4.31	0.18
M2O1	0.25	0.50	0.0657	0.1962	0.2010	2.364	-1.03	-0.91	2.45	0.42
M2O2	0.23	3.35	0.0722	0.2797	0.4609	2.344	-0.95	-0.40	4.70	0.20
M2O3	0.19	1.00	0.0772	0.4192	0.3540	2.560	-0.77	-0.51	2.28	0.34
M2O3	0.18	0.70	0.0912	0.3937	0.1742	2.721	-0.73	-0.26	1.69	0.43

obtained by using the last map as a prior information, we have used the high resolution X-ray data on diopside studied by Rossi *et al.* (1987). The results of the topological analysis of the three EDD's are reported in Table 3. In Fig. 1b the $\nabla^2\rho(\mathbf{r})$ at the Si-O bond critical points vs. the bond distance is plotted for the static, the dynamic and the MEM EDD's. While both the value of the ED and the location of bcp is almost the same in the static and the dynamical case (Table 3), the arrangement of the electrons [*i.e.* $\nabla^2\rho(\mathbf{r})$ pattern] around the c.p. is sensitive to the nuclear motion in the dynamical case (as a consequence of the Born-Oppenheimer approximation). These effects are evident when we look at the differences between the values of $\nabla^2\rho(\mathbf{r})$ (Fig. 1b) and the eigenvalues for the λ's in the Hessian matrix of $\rho(\mathbf{r})$ calculated at the c.p.'s (Table 3, Fig. 1c). In general, we observe a systematic increase in the values of $\nabla^2\rho(\mathbf{r})$ and the λ's in the tetrahedral sites and a significant decrease in these values for the octahedral ones (Fig. 1e, d, f, g, h, i).

Given these considerations, one can expect some minor differences between the topology of these different objects. Bearing that in mind, it is our opinion that this kind of study could nevertheless provide a great deal of useful information about the structural and thermodynamic properties in phase transitions, cation ordering and so on.

Topology of bcp in pigeonites

Taking into account that the aim of this study is a methodological analysis of MEM capabilities in Bader topological analyses, we have further attempted some interpretation in a

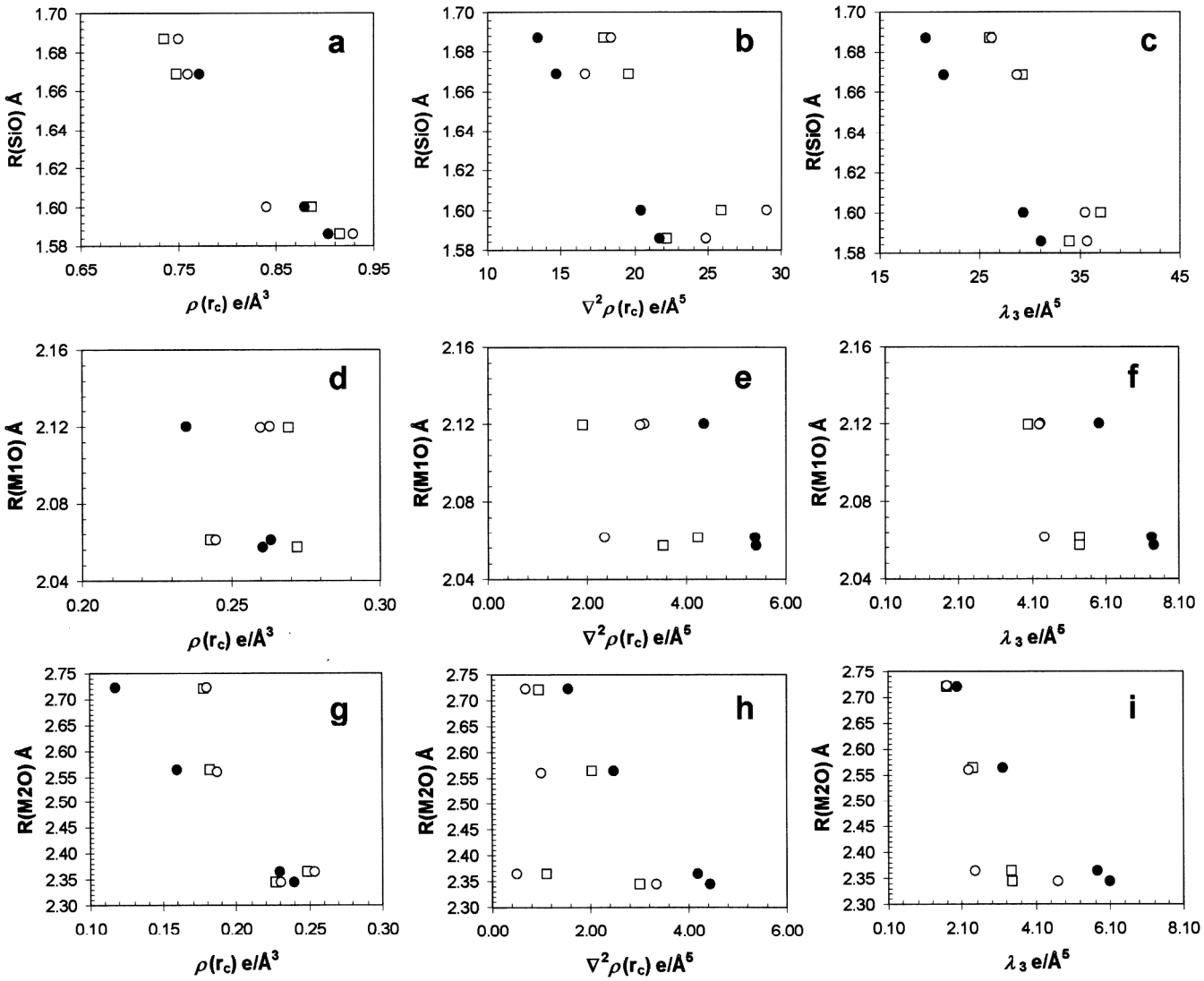

Fig. 1. Bond lengths and bcp properties at the different sites of the diopside structure. Filled circles: procrystal EDD; open squares: dynamic map obtained with procrystal EDD; open circles: MEM EDD obtained from the experimental data of Rossi *et al.* (1987).

crystal-chemical framework. A more complete study, including an overall analysis of every topological quantity, is in progress and will be published later on.

All of the maxima found in the MEM map are in close agreement with those derived from a classical least-squares structure refinement.

The split M2 site observed in the Fourier difference maps (M21 site) can be interpreted as the Ca and Mg/(Fe) atoms being ordered in different coordinations within the M2 cavity. This agrees well with the peak height found at the M21 site positions in the $\Delta\rho(\mathbf{r})_{MEM}$ maps, since the peak height value is qualitatively higher for crystal BTS-308 n.13 than for crystal Dien2, in accordance with chemical analyses that report a higher Ca-content for crystal BTS-308 n.13. The same feature has already been noticed and previously proposed through differential Fourier synthesis in diopside (Rossi *et al.*, 1987; Tribaudino *et al.*, 1989) and recently studied by the same method along the diopside-enstatite join by Tribaudino& Nestola (2002). We should observe that in the samples of this study, TEM observations exclude the presence of exsolution as the reason for these features in the electron density (Pasqual *et al.*, 2000; Tribaudino *et al.*, 2002).

The values of $\rho(\mathbf{r})$, $\nabla^2\rho(\mathbf{r})$ and the coordinates of the c.p.'s for bonded directions involving the tetrahedral sites, as found in the MEM EDD's, are reported in Table 4a and 4b for BTS-308 n.13 and Dien2, respectively. The bonded radii of oxygen, *i.e.* the distances between the bcp's and the position of the oxygen atoms [r(O)], and the angles between the cations, the bcp and the anions are also reported. The values of $\rho(\mathbf{r})$, $\nabla^2\rho(\mathbf{r})$ and λ_3 correlate negatively with the tetrahedral bond distances (Fig. 2a, b and c), and the values of $\rho(\mathbf{r})$ and $\nabla^2\rho(\mathbf{r})$ correlate positively, as previously observed by Gibbs *et al.* (2001) in *ab initio* modelling of silicate structures. We also found that λ_3 is larger than $|\lambda_1+\lambda_2|$, although λ_2 is systematically smaller than λ_1. There is also an inverse linear correlation between $\rho(\mathbf{r})$ and r(O). Mean $\nabla^2\rho(\mathbf{r})$ values for each tetrahedron are similar to those obtained

Table 4. Values of $\rho(r)$ (e/Å^3), of $\nabla^2\rho$ (e/Å^5), and fractional coordinates of the critical points of tetrahedral bonds in BTS-308 n.13 and Dien n.2. The bond-length (Å), eigenvalues of the hessian matrix (e/Å^5), the ratios $|\lambda_1|/\lambda_3$, the angle between the nuclei involved and the bcp (°), as well as the electronegativities (see text) are also reported.

BTS-308 n.13	$\rho(\mathbf{r})$	$\nabla^2\rho(\mathbf{r})$	*x*	*y*	*z*	R(SiO)	λ_1	λ_2	λ_3	$\lvert\lambda_1\rvert/\lambda_3$	angle	R(O)	χ_M
SiA-O1A	0.820	26.11	-0.0358	0.3417	0.2221	1.6153	-4.98	-4.10	35.20	0.14	174.38	0.8926	1.767
SiA-O2A	0.874	30.40	0.0783	0.4114	0.3054	1.5990	-5.22	-3.26	38.88	0.13	177.30	0.8834	1.798
SiA-O3A	0.732	22.08	0.0731	0.3086	0.4189	1.6613	-3.61	-2.57	28.27	0.13	174.20	0.8988	1.719
SiA-O3A	0.729	21.59	0.0698	0.2942	0.1861	1.6366	-4.73	-3.71	30.03	0.16	178.84	0.8966	1.718
average	0.789	25.05				1.6281	-4.64	-3.41	33.10	0.14	176.18	0.8929	1.751
SiB-O1B	0.808	25.41	0.4705	0.8416	0.1898	1.6208	-5.11	-4.42	34.95	0.15	174.04	0.8932	1.761
SiB-O2B	0.900	27.09	0.5838	0.9036	0.3069	1.6017	-6.03	-4.72	37.85	0.16	173.26	0.8865	1.808
SiB-O3B	0.691	19.29	0.5785	0.7800	0.3490	1.6720	-4.51	-3.42	27.22	0.17	174.92	0.9153	1.689
SiB-O3B	0.680	18.97	0.5732	0.8192	0.1206	1.6633	-5.03	-4.16	18.16	0.28	176.57	0.9190	1.681
average	0.770	22.69				1.6395	-5.17	-4.18	29.55	0.19	170.58	0.9035	1.735
Dien n.2	$\rho(\mathbf{r})$	$\nabla^2\rho(\mathbf{r})$	*x*	*y*	*z*	R(SiO)	λ_1	λ_2	λ_3	$\lvert\lambda_1\rvert/\lambda_3$	angle	R(O)	χ_M
SiA-O1A	0.886	21.99	-0.0357	0.3441	0.2417	1.610	-8.64	-5.75	36.38	0.24	174.89	0.8963	1.797
SiA-O2A	0.885	29.24	0.0771	0.4136	0.3039	1.588	-5.67	-2.97	37.89	0.15	178.30	0.8733	1.807
SiA-O3A	0.762	19.88	0.0719	0.3165	0.4271	1.680	-6.26	-4.12	30.27	0.21	174.18	0.9450	1.715
SiA-O3A	0.772	20.46	0.0711	0.2896	0.2103	1.654	-7.21	-5.80	33.47	0.22	176.81	0.9368	1.723
average	0.826	22.89				1.633	-6.95	-4.66	34.50	0.20	176.05	0.9129	1.761
SiB-O1B	0.848	25.54	0.4722	0.8417	0.1827	1.615	-5.66	-4.35	35.55	0.16	175.62	0.8963	1.779
SiB-O2B	0.856	27.09	0.5852	0.9045	0.3006	1.590	-6.35	-5.76	39.19	0.16	176.93	0.8788	1.791
SiB-O3B	0.750	18.10	0.5782	0.7771	0.3326	1.683	-6.25	-4.30	28.65	0.22	174.45	0.9417	1.710
SiB-O3B	0.695	23.72	0.5741	0.8223	0.1166	1.685	-5.12	-4.24	33.09	0.15	178.84	0.9581	1.674
average	0.787	23.61				1.643	-5.85	-4.66	34.12	0.17	176.46	0.9187	1.738

tained for diopside (22.25 e/Å^5) and slightly higher than in the procrystal EDD of diopside (17.58 e/Å^5). The main difference is found in the mean value of λ_3 for the B tetrahedron of crystal BTS-308 n.13, which is significantly lower than the mean values obtained for the A tetrahedron of the same crystal and both tetrehadra of crystal Dien n.2. We ascribe this depletion of charge along the bond path as the consequence of the very limited $Si_{-1}Al$ substitution in the B tetrahedron of crystal BTS-308 n.13, according to mean bond distances and chemical composition. The bcp's within this tetrahedron that contribute to decreasing the mean value of λ_3 are those present in the bond path of the Si-O3 bonds.

The properties of bcp in the octahedral sites M1, M2 are reported in Table 5a and 5b for BTS-308 n.13 and Dien2, respectively. Tables 4 and 5 also report the bonded radii of oxygen, *i.e.* the distances between the cps and the position of the oxygen atoms, and the angles between the cations, the bcp and the anions.

In situ electronegativities of the cations (χ_M) have been calculated with the following expression (Allen, 1989):

$$\chi_M = 1.31 \times \{[N_M \times \rho(\mathbf{r})]/r(O)\}^{0.23}$$

where N_M is the number of valence electrons. These values for the tetrahedral and octahedral sites are also reported in Tables 4 and 5. Although this expression applies to ground state atoms we have attempted to estimate this magnitude using our time and space average EDD's and compare it with Paling's theoretical values. The mean values obtained for the tetrahedral sites (Table 4a and b) agree with Pauling's values within 3-4% and are positively correlated with $\rho(\mathbf{r})$ (Fig. 3a). We instead found larger discrepancies for the χ_M value at M1 in Dien n.2, which is exclusively occupied by Mg and is nevertheless 10% lower than Pauling's value for Mg (1.2). Electronegativities for octahedral sites also correlate positively with $\rho(\mathbf{r})$ values (Fig. 3b and c). Similar positive correlations have been found in zeolites by Kirfel & Gibbs (2000), although the trends were poorer.

The most important features to be noticed can be summarised as follows:

1. The refined site scattering (s.s.) at the M1 site is 15.11 electrons per formula unit (epfu) for BTS-308 n.13 and 12 epfu for Dien2, and the mean $\rho(\mathbf{r})$ value (Table 5) at the bcp is greater for BTS-308 n.13 than for Dien2, as expected. Despite the differences between the electron densities, the $\nabla^2\rho(\mathbf{r})$ values at the bcc's are very similar. Therefore, they do not seem to be too sensitive to the composition. Nevertheless, we cannot say anything about the local virial re-arrangement of the electrons at this c.p.

2. The ED values at the bcp's in the M2 sites are proportionally higher for BTS-308 n.13 than for Dien n.2, because of the higher site scattering (22.93 epfu *vs* 13.28 epfu, respectively). Looking at the average Laplacian value for the bcp's at the M2 site, higher values are recorded for the M2 site of crystal BTS-308 n.13 with respect to Dien2 for the same atom site, indicating a relative depletion of charge for the M2 site of crystal BTS-308 n.13. The most surprising feature to notice is the presence in Dien2 of a (3,-1) bcp characterised by a negative value of $\nabla^2\rho(\mathbf{r})$. We should remember that the anion involved in this outlying bond is O2B, which has the highest atomic displacement parameter among the oxygen atoms and could be split into two anion positions, as suggested by Tribaudino & Nestola (2002).

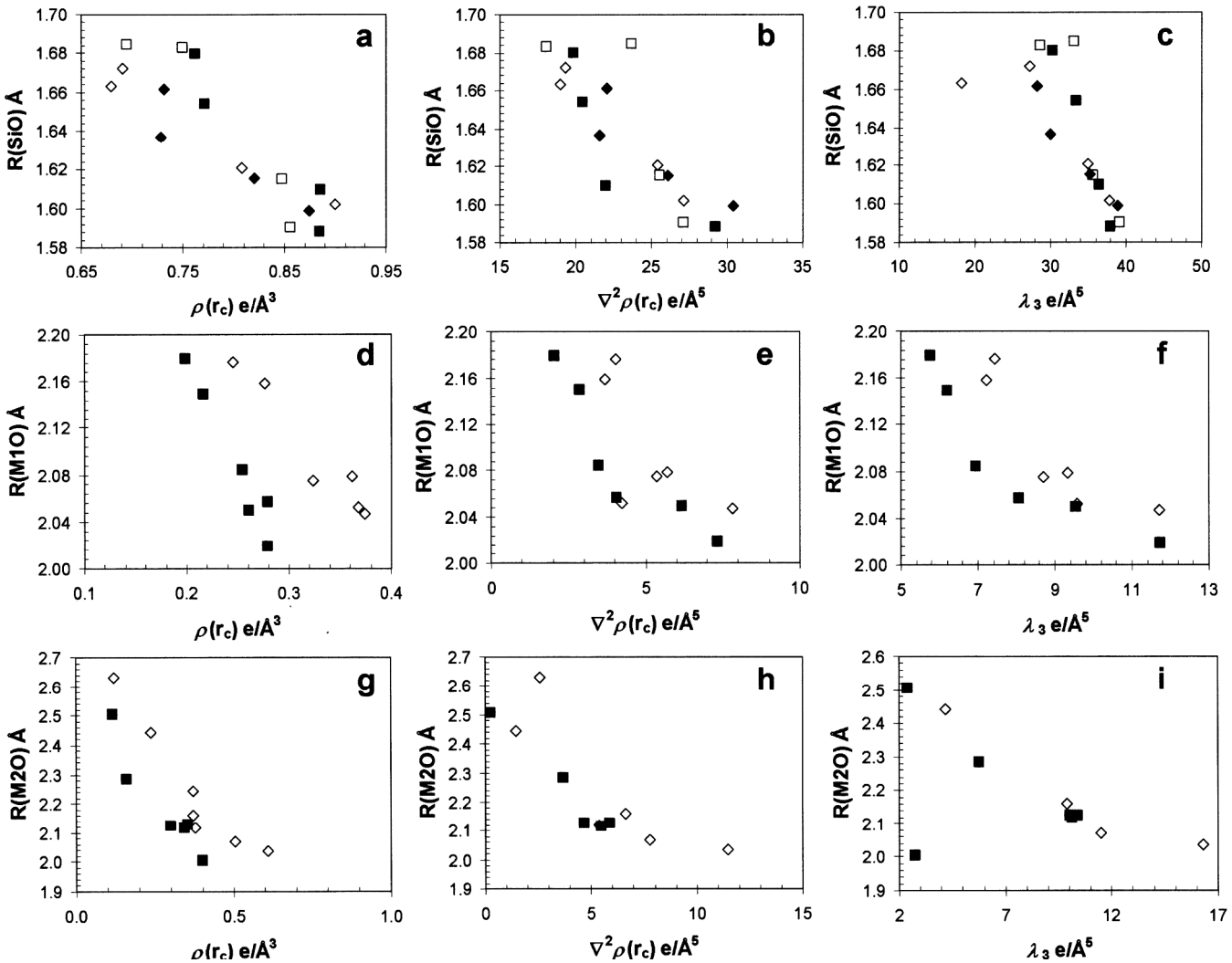

Fig. 2. Bond lengths and bcp properties at the different sites of the studied crystals of pigeonite. Squares: Dien2; diamonds: BTS-308 n.13. In figs. a, b and c: filled symbols correspond to bcp within the A chain tetrahedron; open symbols correspond to bcp within the B chain tetrahedron).

3. We found the same bcp's for both the M2 and M21 site, indicating that the bcp's we have found represent the space-average topology for this site. It seems that the mean bond paths in split sites show the same attractor. Further characterisation of this interesting feature should be done through a careful study of the gradient paths at this site.

4. The mean coordination in both the M2 and the M21 sites is 6-fold in the pigeonites of this study. However, due to the structural changes from the displacive $P2_1/c \leftrightarrow C2/c$ phase transition in both crystals (Cámara *et al.*, 2002; Tribaudino *et al.*, 2002), we cannot exclude that this mean coordination could change as the temperature approaches the critical temperature for the phase transition. In fact, Downs (2003) describes a change of bonding topologies accompanying the $P2_1/c \leftrightarrow C2/c$ phase transition while the site keeps its 6-fold coordination in both structures (kanoite), grows from 5-fold to 6-fold coordination (spodumene) or from 4-fold to 6-fold (clinoferrosilite, $LiScSi_2O_6$, $LiFeSi_2O_6$).

In light of the above considerations, the main differences between both crystals studied concern the topology of the bcp at the M2 sites. In particular, the ellipticities ($|\lambda_1|/\lambda_3$) of the M2 site are significantly larger for crystal Dien n.2 than for crystal BTS-308 n.13, thus indicating lower bond strength and/or more ionic character for the M2 site of Ca-poor crystal. This could explain the discontinuous character and the higher T_c found for the $P2_1/c \leftrightarrow C2/c$ phase transition in this crystal (Tribaudino *et al.*, 2002) when compared to the continuous character found in other crystals of sample BTS-308 by Cámara *et al.* (2002). This interesting feature might explain the thermodynamic change of properties of the material. In fact, it has already been suggested by Arlt *et al.* (1998) that chemical substitutions involving different electronic settings at octahedral sites in $P2_1/c$ pyroxenes can change the stability field of the high pressure $C2/c$ phase (see Fig. 3 in Arlt *et al.*, 1998). In that particular case, the authors justify the additional stability of the HP phase as a consequence of the presence of crystal field stabilisation energy (CFSE) due to the presence of Cr or Fe.

In conclusion, the study of an accurate MEM EDD can readily express valuable information about the topology of

Table 5. Values of ρ(r) (e/Å^3), of $\nabla^2\rho$ (e/Å^5), and fractional coordinates of the critical points of the M1 and M2 sites in BTS-308 n.13 and Dien n.2. The bond-length (Å), eigenvalues of the hessian matrix (e/Å^5), the ratios $|\lambda_1|/\lambda_3$, the angle between the nuclei involved and the bcp, as well as the electronegativities (see text) are also reported.

BTS-308 n.13	ρ(**r**)	$\nabla^2\rho$(**r**)	*x*	*y*	*z*	R(MO)	λ_1	λ_2	λ_3	$\lvert\lambda_1\rvert/\lambda_3$	angle	R(O)	χ_M
M1-O1A	0.276	3.68	0.1953	0.7409	0.2743	2.1587	-2.61	-0.93	7.21	0.36	177.95	1.160	1.104
M1-O1A	0.368	4.24	0.1972	0.6573	0.0436	2.0522	-2.97	-2.36	9.57	0.31	177.69	1.090	1.197
M1-O1B	0.245	4.02	0.3090	0.7386	0.1863	2.1764	-2.13	-1.28	7.44	0.29	178.55	1.160	1.074
M1-O1B	0.324	5.35	0.3079	0.6570	0.4209	2.0752	-2.06	-1.27	8.69	0.24	178.30	1.100	1.160
M1-O2A	0.374	7.81	0.1923	0.5815	0.2734	2.0474	-2.54	-1.36	11.70	0.22	176.39	1.110	1.196
M1-O2B	0.362	5.69	0.3047	0.5750	0.1894	2.0789	-2.21	-1.42	9.32	0.24	174.86	1.130	1.183
average	0.325	5.13				2.0981	-2.42	-1.44	8.99	0.27	177.29	1.125	1.152
M2-O1A	0.371	6.65	0.1960	-0.0724	0.2746	2.1595	-1.91	-1.35	9.91	0.19	177.45	1.110	1.194
M2-O1B	0.377	5.40	0.3135	-0.0750	0.1901	2.1181	-2.77	-1.90	10.07	0.28	174.35	1.077	1.207
M2-O2A	0.504	7.79	0.1909	0.0109	0.0292	2.0698	-2.54	-1.18	11.51	0.22	176.37	1.040	1.301
M2-O2B	0.609	11.47	0.3117	0.0252	0.4271	2.0358	-2.52	-2.27	16.28	0.15	168.86	1.020	1.365
M2-O3A	0.237	1.44	0.1786	0.1261	0.1664	2.4425	-1.70	-1.04	4.18	0.41	173.00	1.230	1.052
M2-O3B	0.121	2.59	0.3244	0.1085	0.1197	2.6305	-0.70	-0.09	3.38	0.21	176.95	1.330	0.885
average	0.370	5.89				2.2427	-2.02	-1.31	9.22	0.24	174.50	1.135	1.167
Dien n.2	ρ(**r**)	$\nabla^2\rho$(**r**)	*x*	*y*	*z*	R(MO)	λ_1	λ_2	λ_3	$\lvert\lambda_1\rvert/\lambda_3$	angle	R(O)	χ_M
M1-O1A	0.217	2.88	0.2004	0.7395	0.2599	2.1495	-2.70	-0.62	6.20	0.44	174.46	1.200	1.037
M1-O1A	0.279	4.07	0.2003	0.6568	0.0451	2.0567	-2.44	-1.58	8.08	0.30	178.56	1.150	1.109
M1-O1B	0.199	2.05	0.3069	0.7333	0.1776	2.1793	-2.40	-1.31	5.76	0.42	176.43	1.220	1.012
M1-O1B	0.255	3.48	0.3047	0.6548	0.4036	2.0840	-2.27	-1.20	6.95	0.33	177.68	1.160	1.084
M1-O2A	0.279	7.34	0.1960	0.5848	0.2668	2.0193	-2.54	-1.87	11.75	0.22	177.06	1.135	1.113
M1-O2B	0.261	6.18	0.3030	0.5790	0.1789	2.0495	-2.32	-1.06	9.56	0.24	178.71	1.150	1.092
average	0.248	4.33				2.0897	-2.45	-1.27	8.05	0.32	177.15	1.169	1.075
M2-O1A	0.303	4.69	0.1975	-0.0698	0.2533	2.1255	-3.47	-2.25	10.40	0.33	168.97	1.140	1.132
M2-O1B	0.355	5.90	0.3099	-0.0675	0.1756	2.1264	-3.29	-0.88	10.07	0.33	177.45	1.110	1.182
M2-O2A	0.346	5.50	0.1910	0.0059	0.0289	2.1159	-3.33	-1.32	10.16	0.33	176.11	1.080	1.182
M2-O2B	0.402	-2.51	0.3013	0.0101	0.3949	2.0039	-4.10	-1.16	2.76	1.49	171.98	1.150	1.206
M2-O3A	0.162	3.69	0.1826	0.1072	0.1615	2.2834	-1.31	-0.76	5.76	0.23	173.04	1.260	0.959
M2-O3B	0.119	0.26	0.3195	0.1106	0.1556	2.5052	-1.30	-0.85	2.42	0.54	169.86	1.360	0.876
average	0.281	2.92				2.1934	-2.80	-1.20	6.93	0.54	172.90	1.183	1.090

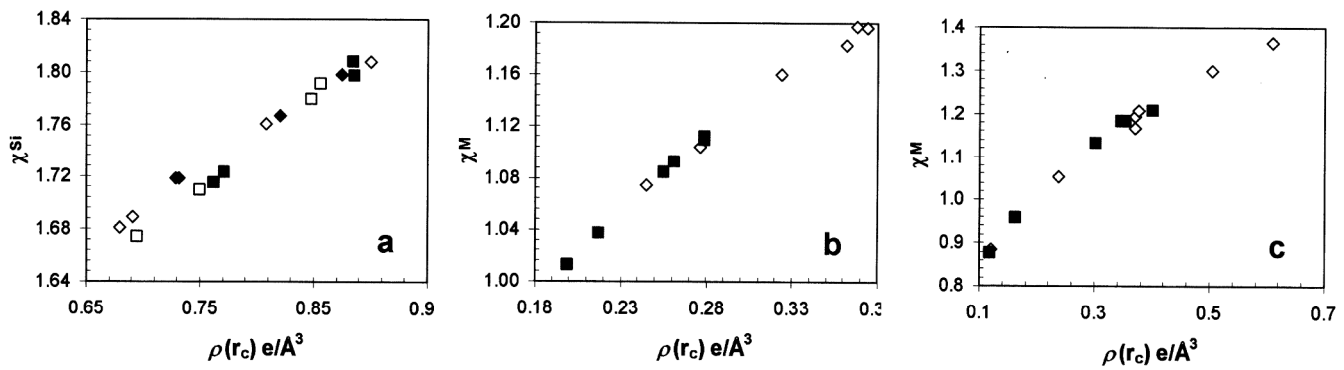

Fig. 3. Cation electronegativities and ρ(**r**) values at the different sites of the pigeonite structures. Symbols as in Fig. 2.

complex solid solutions that can be directly discussed on the same basis of a standard analysis of the EDD as presented in Bader (1990). Further developments are expected on the calculations of the MEM EDD algorithm and, from a mineralogical application viewpoint, on the further calculations of useful physical quantities that could be obtained from the MEM EDD's, thereby opening new horizons in the field of Mineral Sciences.

Acknowledgements: The authors are indebted to Luciano Ungaretti, who strongly encouraged this kind of approach in the field of Mineral Sciences in the last years of his life. We would also like to thank Daria Pasqual (University of Modena, Italy) for providing the Paraná rhyodacite sample. Financial support from the CNR and MURST project "Transformation, reactions, ordering in minerals" is gratefully acknowledged.

References

Allen, L.C. (1989): Electronegativity is the average one-electron energy of the valence-shell electrons in ground state free atoms. *J. Am. Chem. Soc.*, **111**, 9003-9014.

Angel, R.J., Chopelas, A., Ross, N.L. (1992): Stability of high-density clinoenstatite at upper mantle pressures. *Nature*, **358**, 322-324.

Arlt, T, Angel, R.J., Miletich, R., Armbruster, T., Peters, T. (1998): High pressure $P2_1/c$-$C2/c$ phase transitions in clinopyroxenes: influence of cation size and electronic structure. *Am. Mineral.*, **83**, 1176-1181.

Bader, R.F.W. (1990): Atoms in molecules: a quantum theory. Clarendon Press, Oxford.

– (1998): A bond path: A universal indicator of bonded interactions. *J. Phys. Chem.*, **102A**, 7314-7323.

Bader, R.F.W. & Essen, H. (1984): The characterisation of atomic interactions. *J. Chem. Phys.*, **80**, 1943-1959.

Bianchi, R., Gervasio, G., Marabello, D. (2001): Experimental electron density in the triclinic phase of $Co_2(CO)_6(-CO)(-C_4O_2H_2)$ at 120 K. *Acta Crystallogr.*, **B57**, 638-645.

Bricogne, G. (1984): Maximum entropy and the foundations of direct methods. *Acta Crystallogr.*, **A40**, 410-445.

Brown, G.E., Prewitt, C.T., Papike, J.J., Sueno, S. (1972): A comparison of the structures of low and high pigeonite. *J. Geophys. Research*, **77**, 5778-5789.

Cámara, F., Carpenter, M.A., Domeneghetti, M.C., Tazzoli, V. (2002): Non-convergent ordering and displacive phase transition in pigeonite: in-situ HT XRD study. *Phys. Chem. Minerals*, **29**, 331-340.

Collins, D.M. (1982): Electron density images from imperfect data by iterative entropy maximization. *Nature*, **298**, 49-51.

Coppens, P. (1997): X-ray charge densities and chemical bonding. Oxford University Press.

Dove, M.T. (2001): Computer simulations of solid solutions. *in* "Solid solutions in silicate and oxyde systems. EMU notes in Mineralogy, vol. 3". C.A. Geiger ed. Eötvös University Press, Budapest.

Downs, R.T. (2003): Topology of the pyroxenes as a function of temperature, pressure, and composition as determined from the procrystal electron density. *Am. Mineral.*, **88**, 556-566.

Downs, R.T., Andalman, A., Hudasko, M. (1996): The coordination numbers of Na and K atoms in low albite and microcline as determined from a procrystal electron-density distribution. *Am. Mineral.*, **81**, 1344-1349.

Downs, R.T., Gibbs, G.V., Boisen, M.B. Jr., Rosso, K.M. (2002): A comparison of procrystal and ab initio model representations of the electron-density distributions of minerals. *Phys. Chem. Minerals*, **29**, 369-385.

Gibbs, G.V., Boisen, M.B. Jr., Beverly, L.L., Rosso, K.M. (2001): A computational quantum-chemical study of the bonded interactions in Earth materials and structurally and chemically related molecules. *in* "Molecular modelling theory: applications in the geosciences. Reviews in Mineralogy and Geochemistry, vol 42", R.T. Cygan, J.D. Kubicki, J.J. Rosso (series eds), Mineralogical Society of America, Washington, DC.

Hugh-Jones, D.A., Woodland, A.B., Angel, R.J. (1994): The structure of high pressure $C2/c$ ferrosilite and crystal chemistry of high-pressure $C2/c$ pyroxenes. *Am. Mineral.*, **79**, 1032-1041.

Ivanov, Y., Zhurova, E.A., Zhurov, V., Tanaka, K., Tsirelson, V. (1999): Electron density and electrostatic potential of $KNiF_3$: multipole, orbital and topological analyses of vacuum-camera-imaging plate and four-circle diffractometer data. *Acta Crystallogr.*, **B55**, 923-930.

Jauch, W. & Palmer, A. (1993) The maximum-entropy method in charge-density studies: aspects of reliability. *Acta Crystallogr.*, **A49**, 590-591.

Kirfel, A. & Gibbs, G.V. (2000): Experimental electron-density distributions and bonded interactions for fibrous zeolites natrolite, mesolite and scolecite and related materials. *Phys. Chem. Minerals*, **27**, 270-284.

Kumazawa, S., Kubota, Y., Takata, M., Sakata, M. (1993): MEED: a program package for electron-density-distribution calculation by the maximum-entropy method. *J. Appl.* Crystallogr., **26**, 453-457.

Merli, M., Cámara, F., Domeneghetti, M.C., Tazzoli, V. (2002a): Leverage analysis of X-ray single crystal diffraction data from orthopyroxene and pigeonite. *Eur. J. Mineral.*, **14**, 773-784.

Merli, M., Pavese, A., Ranzini, M. (2002b): Study of the electron density in MgO, $(Mg_{0.963}Fe_{0.037})O$ and Cu_2O by Maximum Entropy Method and multipole refinements: comparison between methods. *Phys. Chem. Minerals*, **29**, 455-464.

Palatinus, L. & Van Smaalen, S. (2002): The generalized F constraint in the maximum-entropy method – a study on simulated data. *Acta Crystallogr.*, **A 58**, 559-567.

Pasqual, D., Molin, G., Tribaudino, M. (2000): Single-crystal thermometric calibration of Fe-Mg order-disorder in pigeonites. *Am. Mineral.*, **85**, 953-962.

Prewitt, C.T., Brown, G.E., Papike, J.J. (1971): Apollo 12 clinopyroxenes. High temperature X-ray diffraction studies. *Geochim. Cosmochim. Acta, Suppl* 2, **1**, 59-68.

Prince, E. (1989): The maximum entropy distribution consistent with observed structure amplitudes. *Acta Crystallogr.*, **A45**, 200-203.

Prince, E., Sjolin, L., Alenljung, R. (1988): Phase extension by combined entropy maximization and solvent flattening. *Acta Crystallogr.*, **A44**, 216-222.

Rossi, G., Oberti, R., Dal Negro, A., Molin, G.M., Mellini, M. (1987): Residual electron density of the M2 site in $C2/c$ clinopyroxenes relationship with bulk chemistry and sub-solidus evolution. *Phys. Chem. Minerals*, **14**, 514-520.

Roversi, P., Irwin, J.J., Bricogne, G. (1998): Accurate charge density studies as an extension of Bayesian crystal structure determination. *Acta Crystallogr.*, **A54**, 971-996.

Sakata, M. & Sato, M. (1990): Accurate structure analysis by the maximum entropy method. *Acta Crystallogr.*, **A46**, 263-270.

Shannon, C.E. & Weaver, W. (1949): The mathematical theory of communication. University of Illinois Press, Urbana.

Sueno, S., Kimata, M., Prewitt, C.T. (1984): The crystal structure of high clinoferrosilite. *Am. Mineral.*, **69**, 264-269.

Tribaudino, M., Benna, P., Bruno, E. (1989): Average structure and M2 site configurations in $C2/c$ clinopyroxenes along the Di-En join. *Contrib. Mineral. Petrol.*, **103**, 452-456.

Tribaudino, M. & Nestola, F. (2002): Average and local structure in $P2_1/c$ clinopyroxenes along the join diopside-enstatite ($CaMgSi_2O_6$-$Mg_2Si_2O_6$). *Eur. J. Mineral.*, **14**, 549-555.

Tribaudino, M., Nestola, F., Cámara, F., Domeneghetti, M.C. (2002): The high-temperature $P2_1/c$-$C2/c$ phase transition in Fe-free pyroxene ($Ca_{0.15}Mg_{1.85}Si_2O_6$): structural and thermodynamic behavior. *Am. Mineral.*, **87**, 648-657.

Received 20 February 2002
Modified version received 10 February 2003
Accepted 16 May 2003